Picosecond acoustics for mass characterization of nanoparticles on thin membranes

E. Glushkov,[1] N. Glushkova,[1] F. Soldevila,[2] L. Belliard,[2] S. Baltogiannis,[2] P. Paćko,[3] S. Jo,[4] A. Mihi,[4] D. Torrent,[5] and O. Boyko[2,*]

[1] *Kuban State University, Institute for Mathematics, Mechanics, and Informatics, 350080 Krasnodar, Russia*
[2] *Sorbonne Université, CNRS, Institut des Nanosciences de Paris, INSP, F-75005 Paris, France*
[3] *Department of Manufacturing Systems, AGH University of Kraków, Poland*
[4] *Institute of Materials Science of Barcelona (ICMAB-CSIC), Campus de la UAB, 08193 Bellaterra, Spain*
[5] *GROC·UJI, Institute of New Imaging Technologies (INIT), Universitat Jaume I, Castelló, Spain*

(Received 11 February 2025; revised 16 September 2025; accepted 16 October 2025; published 7 November 2025)

In this paper, we demonstrate the potential of laser picosecond acoustics for characterizing the averaged mass of nanoparticles distributed on the surface of submicron-thin membranes. Specifically, we investigate guided-wave (GW) propagation in thin membranes covered with silicon oxide nanospheres. By employing picosecond acoustics, we excite and detect GWs, generating spatiotemporal maps of acoustic behavior that visualize the GW dispersion curves. Such dispersion curves are also calculated using a computer model, which implements a semianalytical Green's-matrix-based solution to the corresponding boundary-value problem. Based on these data, inverse problems are solved to determine the effective elastic parameters of the membrane and the average mass of particles per unit surface. The method exhibits high sensitivity in detecting masses as small as 200 femtograms per square micron. The wide field of view provided by the picosecond technique enables efficient scanning of millimetric surfaces with the potential to detect mass variations at the hundred-femtogram level over large areas.

DOI: 10.1103/7d7h-qfxx

I. INTRODUCTION

The precise measurement of nanoparticle masses is of paramount importance for advancing technologies in materials science, nanotechnology, and biophysics. As devices become increasingly miniaturized and nanostructures are more deeply integrated into functional materials, the demand for accurate, noninvasive mass measurement techniques has reached an unprecedented level. Traditional approaches to nanoparticle characterization, such as transmission electron microscopy (TEM) [1] and energy-dispersive X-ray spectroscopy (EDS) [2], are widely employed but come with inherent limitations. TEM, while offering high spatial resolution for structural imaging, requires labor-intensive sample preparation and provides only indirect mass estimates. Similarly, EDS effectively quantifies elemental composition but struggles to accurately determine nanoparticle mass, especially on complex or heterogeneous surfaces. These constraints highlight the necessity for more versatile and precise methodologies.

When dealing with uniform nanoparticle distributions, techniques such as the quartz crystal microbalance [3] or ellipsometry [4] provide reliable and efficient alternatives. Quartz crystal microbalance methods, rooted in the Sauerbrey equation, have demonstrated considerable potential for mass detection through the measurement of frequency shifts induced by deposited particles. However, these methods are constrained by their dependence on planar, homogeneous substrates and are less effective at resolving nanoscale mass distributions or complex geometries.

Emerging acoustic methods, particularly those utilizing guided waves (GWs), such as surface acoustic waves (SAWs) or Lamb waves, present a promising solution to measure sparse nanoparticles distributed on a flat surface. Guided waves are elastic waves, the propagation characteristics of which are sensitive to variations in the medium's properties, e.g., surface mass distribution. This sensitivity makes GWs particularly well suited for nanoscale characterization. Deposition of nanoparticles on a substrate leads to detectable changes in the GW velocity and dispersion. These perturbations are harnessed to infer nanoparticle mass with remarkable precision. Specifically, GW-based devices exploit the relationship between wave propagation parameters—such as phase velocity, amplitude, and frequency—and the added mass to deduce highly accurate measurements. Thus, traditional GW devices [5,6]

*Contact author: olga.boyko@insp.jussieu.fr

often rely on interdigitated transducers (IDTs) to generate waves, which limits their applicability to specific materials and device configurations. These limitations highlight the pressing need for innovative techniques to overcome these challenges, particularly in the realm of high-frequency devices. Such advancements could enhance processing speeds to handle significantly larger volumes of information in data transmission systems, enable operations in the quantum regime, or substantially improve sensor sensitivity [7].

Building on the principles of GW-based sensing, laser picosecond acoustics has emerged as a promising tool for characterizing microparticle and nanoparticle systems. Unlike traditional methods, it eliminates the need for complex high-tech fabrication processes associated with IDTs, making it a versatile and accessible option for laboratory applications. This pump-probe technique uses ultrafast optical pulses to excite and detect gigahertz SAWs over a wide frequency range, enabling high-resolution spatiotemporal mapping of wave propagation [8]. Unlike conventional devices that rely on physical transducers, picosecond acoustics employs noninvasive optical methods, making it ideal for studying nanoscale systems and fragile substrates. By avoiding mechanical contact and offering high temporal resolution, this technique achieves exceptional sensitivity and versatility, advancing nanoparticle mass characterization.

In this study, we apply picosecond acoustics to investigate the mass distribution of nanoparticles on thin membranes. Specifically, we consider silicon oxide nanospheres embedded on gold-coated silicon nitride membranes (Fig. 1). Through the analysis of GW propagation in these samples, we have found that their dispersion characteristics are sensitive to the particle mass variation, allowing their detection down to 200 femtograms per square micron. This positions this method among the most sensitive techniques available for nanoparticle mass measurement.

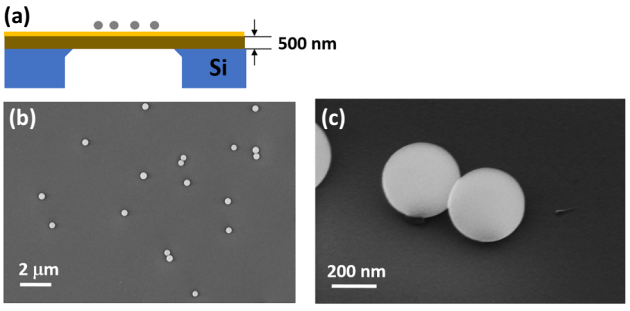

FIG. 1. (a) Schematic of Au/Si_3N_4 bilayer micromembrane with SiO_2 microspheres. (b) Scanning electron microscope (SEM) image showing the distribution of SiO_2 microspheres on the membrane surface, with a scale bar of 2 μm. (c) Side-view SEM image of isolated SiO_2 microspheres, highlighting their spherical morphology, with a scale bar of 200 nm.

Moreover, the findings presented in this work extend beyond simple mass measurement. We highlight the potential of picosecond acoustics for probing mass gradients and other nanoscale phenomena, offering a powerful approach for advanced material characterization. This integration of experimental precision with robust theoretical modeling bridges the gap between fundamental acoustic principles and practical applications, laying the groundwork for innovative solutions in nanoscale mass characterization and beyond [9–11].

II. PICOSECOND MEASUREMENTS

The noninvasive technique of picosecond acoustics is a pump-probe method that enables contactless excitation and detection of elastic waves in a broad frequency range from megahertz to several gigahertz. A schematic of the experimental setup is presented in Fig. 2(a). The experiment employed an ultrafast pulsed laser (Chameleon Ultra II, Coherent Inc.) capable of generating 140-fs pulses with a central wavelength of 800 nm and a repetition rate of 80 MHz. The laser beam was split into two distinct paths: one serving as the pump beam to excite GWs and the other as the probe beam for detection. The splitting was achieved using polarization optics, including a half-wave plate and a polarizing beam splitter (PBS).

The pump beam was temporally modulated using an acousto-optic modulator (AOM) operating at 1.6 MHz, facilitating homodyne detection through a lock-in amplifier (SR865A 4 MHz, Stanford Research Systems). After modulation by the AOM, the pump beam was focused into a β-barium borate (BBO) nonlinear crystal, where its

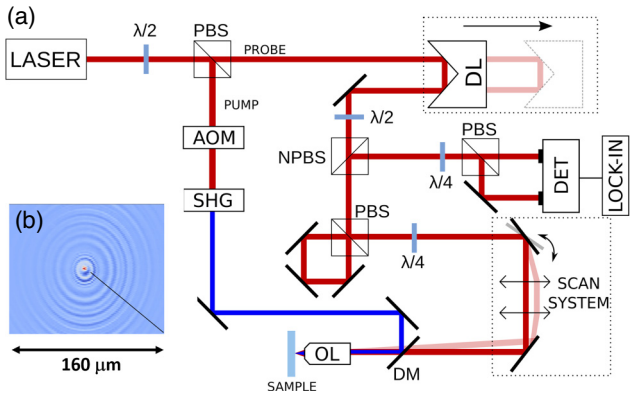

FIG. 2. Gigahertz acoustic-wave generation with ultrashort light pulses. (a) Experimental setup: λ/2, half-wave plate; PBS, polarizing beam splitter; DL, delay line; NPBS, nonpolarizing beam splitter; AOM, acousto-optic modulator; λ/4, quarter-wave plate; OL, objective lens; DET, balanced photodetector; and SHG, second-harmonic-generation crystal. (b) Surface displacement map for a given delay time between the pump and the probe pulses. The black line corresponds to the direction along which we perform our spatiotemporal scans.

wavelength was reduced to 400 nm by two-photon absorption. The beam was then focused onto the sample surface using a high-numerical-aperture objective lens (Nikon CFI Plan Achro Ncg 100× NA 0.9 WD 1.0 mm MRL03901).

The probe beam was used to detect surface displacements induced by the GWs. After being split at the PBS, the probe beam passed through a variable-length delay line [8], which controlled the temporal offset between the pump and probe pulses as they arrived at the sample. It was then directed through a Sagnac interferometer, enabling precise detection of minute variations in the real and imaginary components of the surface reflectivity [10], and then focused onto the sample using the same microscope objective as for the pump beam. To facilitate surface scanning, a two-axis mirror system (Fast Steering Mirrors FMS-300-02, Newport) combined with a telecentric lens system was used. This setup allowed for lateral scanning and the acquisition of two-dimensional (2D) surface velocity maps at arbitrary time intervals between consecutive pump pulses. In this configuration, the effective positioning precision at the sample surface is on the order of ±100 nm. An example of such a map is shown in Fig. 2(b), demonstrating GW propagation across the membrane surface with dispersion-induced wavefront divergence. The reflection-based geometry utilized in this experiment is simple and particularly well suited for nontransparent samples, as both the pump and probe beams interact with the sample from the same side. This configuration broadens the range of materials that can be studied using this approach.

The sample consisted of a silicon nitride (Si_3N_4) membrane coated with a thin gold (Au) layer. The gold film acted as an optoacoustic transducer, absorbing the pump beam's energy and generating GWs in the two-layer Au/Si_3N_4 waveguide [Fig. 1(a)]. The Si_3N_4 membranes (500 nm thick) suspended on a frame were purchased from Silson [12]. The membrane grown by chemical vapor deposition floats in the air, surrounded by a wet-etched Si frame. The substrate dimensions are 10×10 mm^2, with a frame size of 3×3 mm^2. The 100-nm Au film was deposited by a thermal evaporator on all membranes to facilitate optoacoustic characterization. For mass measurements, the membranes were sparsely decorated with SiO_2 microspheres, each 500 nm in diameter. These microspheres were synthesized using the well-established Stöber method [13], ensuring precise control over their size and uniformity. To deposit the spheres onto the membrane surface, a 0.01% (w/v) dispersion of SiO_2 in ethanol was prepared. A volume of 100 μl of this dispersion was applied via spin coating at 2000 revolutions per minute, achieving an even and sparse distribution of the microspheres.

The measurements were carried out for increasing doses of this nanoparticle dispersion. Below, we illustrate the results by examples of measurements and numerical simulation for three membrane loading cases: free, slightly loaded, and heavily loaded membrane [without particles, one dose (two drops) of dispersion, and tens of doses, respectively].

III. GUIDED WAVES

The GWs generated by a pump pulse [see Fig. 2(b)] are Lamb waves propagating in the Au/Si_3N_4 membrane (free elastic bilayer guide). They are excited by a surface load $\mathbf{q}$ resulting from the thermoelastic response to the laser beam. To simulate the frequency spectrum $\mathbf{u}(\mathbf{x},f)$ of the generated displacement field $\mathbf{u}(\mathbf{x},t)$, we use a semianalytic solution to the corresponding boundary-value problem (BVP) for a forced steady-state time-harmonic oscillation $\mathbf{u}e^{-i\omega t}$ of the elastic layered structure considered; here, $\omega = 2\pi f$ is the angular frequency, f is the frequency, the coordinate plane (x,y) coincides with the membrane surface $z = 0$, and the z axis is its outward normal.

Since measurements are performed along a line, we consider a 2D BVP for the in-plane displacement $\mathbf{u} = (u_x, u_z)$, $\mathbf{x} = (x,z)$, and the line of measurements coincides with the x axis. In this case, a Green's-matrix-based integral representation of the BVP solution detailed in Ref. [14] takes the form of a onefold inverse Fourier path integral [15]:

$$\mathbf{u}(\mathbf{x}) = \mathscr{F}_x^{-1}[\mathbf{U}] = \frac{1}{2\pi}\int_\Gamma K(\alpha,z)\mathbf{Q}(\alpha)e^{-i\alpha x}\,d\alpha. \quad (1)$$

Here $K = \mathscr{F}_x[k(\mathbf{x})]$, $\mathbf{Q} = \mathscr{F}_x[\mathbf{q}(x)]$, and $\mathbf{U} = \mathscr{F}_x[\mathbf{u}] = K\mathbf{Q}$ are Fourier symbols in the wave number-frequency domain (α,f); $\mathscr{F}_x$ is the Fourier transform operator with respect to the horizontal coordinate x; and $k(\mathbf{x}) = (\mathbf{k}_1 \vdots \mathbf{k}_2)$ is the 2×2 Green's matrix. Its columns $\mathbf{k}_j$ are the displacement solution vectors corresponding to the surface point loads $\mathbf{q} = \delta(x)\mathbf{i}_j$ applied along the basic coordinate vectors $\mathbf{i}_1 = (1,0)$ and $\mathbf{i}_2 = (0,1)$, $j = 1,2$; δ is Dirac's delta function. The integration path Γ goes in the complex plane α along the real axis rounding the real poles ζ_n of the matrix K elements in accordance with the principle of limiting absorption.

The residue technique reduces the integral in Eq. (1) to a sum of guided waves:

$$\mathbf{u}(\mathbf{x}) = \sum_{n=1}^{N}\mathbf{a}_n(z)e^{i\zeta_n x} + O(e^{-\operatorname{Im}\zeta_{N+1}x}), \quad x > 0,$$
$$\mathbf{a}_n = -i\operatorname{res}K|_{\alpha=-\zeta_n}\mathbf{Q}(-\zeta_n), \quad \zeta x \gg 1. \quad (2)$$

Here N is the number of terms retained in the expansion. It includes the contribution of all real poles ζ_n and, possibly, several complex ones close to the real axis; ζ is a characteristic wave number. These terms describe source-generated GWs, with the poles ζ_n being their wave numbers. Accordingly, $c_n = \omega/\operatorname{Re}\zeta_n$ are their phase velocities, and $\delta_n = 2\pi\operatorname{Im}\zeta_n/\operatorname{Re}\zeta_n$ are the logarithmic decrements of attenuation.

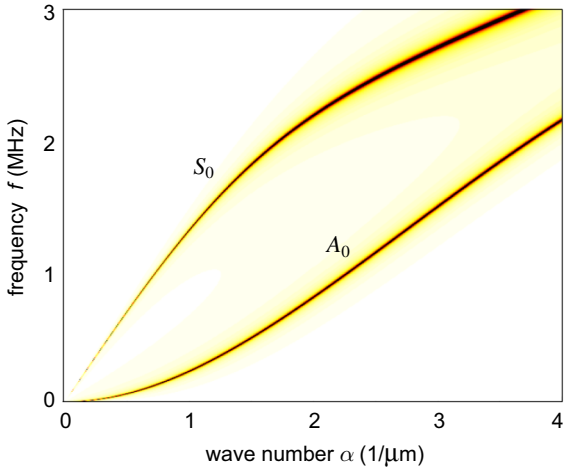

FIG. 3. Level-line image of the $|\omega K_{21}|$ magnitude in the wave number-frequency plane (α, f) computed for the restored effective parameters of the free membrane specified in Table I.

The poles ζ_n are zeros of the common denominator of K elements. They can be obtained as roots of the transcendental equation

$$K_{ij}^{-1}(\alpha, f) = 0, \quad i,j = 1 \text{ or } 2, \tag{3}$$

being, actually, a GW characteristic equation that gives the same dispersion curves $f = f_n(\alpha)$ [or vice versa $\alpha = \zeta_n(f)$] as those obtained in the framework of the conventional modal analysis. These curves can also be visualized by level-line images of $|K_{ij}|$ in the wave number-frequency plane (e.g., $|\omega K_{21}|$ in Fig. 3). The narrow dark bands that follow their ridges visually show them in the plane (α, f).

To estimate the mass of nanoparticles, it is first necessary to quantify the dispersion characteristics of the excited GWs from the measured data.

IV. MEASUREMENT DATA PROCESSING

Probing beam measurements yield records of transient signals $v(x,t) = \dot{u}_z(x,t)$ (velocities of the normal component of surface displacement) stored in arrays $v_{ij} = v(x_i, t_j)$. The signals $v_i(t) = v(x_i, t)$ are acquired at the $N_x + 1$ receiving points $x_i = x_0 + i\Delta x$, $i = 0, 1, 2, \ldots, N_x$ spaced along the x axis with a step Δx. The signals are recorded with a time increment Δt: $t_j = t_0 + j\,\Delta t$, $j = 0, 1, 2, \ldots, N_t$. In the following examples, $\Delta x = 0.416\,\mu$m, $N_x = 255$, $\Delta t = 98.4$ ps, and $N_t = 127$.

The discrete Fourier transform over time t and distance x applied to the arrays v_{ij} yields a so-called H-function that approximates the Fourier symbol $V(\alpha, f) = \mathscr{F}_{xt}[v(x,t)] = -i\omega U_z(\alpha, f)$ of the signal field $v(x,t)$ in the wave number-frequency plane (α, f) [15,16]:

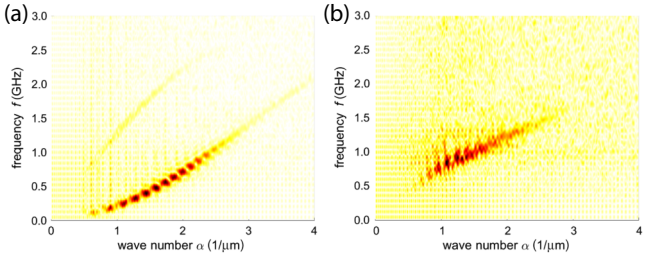

FIG. 4. The H-functions for the data acquired at the free (a) and heavily loaded (b) membranes.

$$H(\alpha, f) = 2\,\Delta x\,\Delta t \left| \sum_{i=0}^{N_x} \sum_{j=0}^{N_t} v_{ij}\, e^{i\omega t_j} \cos \alpha x_i \right|. \tag{4}$$

Figure 4 provides examples of the H-functions obtained for the free and heavily loaded membrane samples under study. It can be seen that, with the rather modest number of measuring points given above, these images are not as sharp as the theoretical scalogram in Fig. 3. The experimental dispersion curve points $(\zeta_n^{\exp}, f_n^{\exp})$ needed for the goal function used to identify effective parameters of the measured sample can hardly be quantified using these data with discernible accuracy. To achieve higher accuracy, we additionally apply the matrix pencil method (MPM) to the data processing [17,18].

Based on the expansion in Eq. (2), the signals' frequency spectra $v_i(f)$ can be written in the form

$$v_i = \sum_{n=1}^{N} b_n \lambda_n^i, \quad i = 0, 1, \ldots, N_x - 1,$$

where $\lambda_n = e^{i\zeta_n \Delta x}$, $b_n = -i\omega a_n e^{i\zeta_n x_0}$, and $a_n = a_{z,n}(0)$. Moving from v_{i-1} to v_i at the next point $x_i = x_{i-1} + \Delta x$ is equivalent to multiplying its terms by λ_n. Accordingly, the matrices V_0 and V_1 of size $(N_x - L) \times L$, which enter the matrix pencil eigenequation

$$V(\lambda) = V_1 - \lambda V_0 = 0, \tag{5}$$

are composed of v_i values at successive L points x_i with a unit shift of the starting point index in each subsequent row; so $L : N \le L \le N_x - L$ is a pencil parameter. For more details on the specific MPM implementation, see Ref. [15].

The complex wave numbers $\zeta_n = \log(\lambda_n)/(i\Delta x)$ are expressed through the eigenvalues λ_n of Eq. (5) and are therefore specified in the range $|\mathrm{Re}\,\zeta_n| < \pi/\Delta x$. Obviously, the experimental data are imperfect, containing noise, reflected waves, and wave interference. Moreover, some GWs are poorly excitable, so that fewer than N

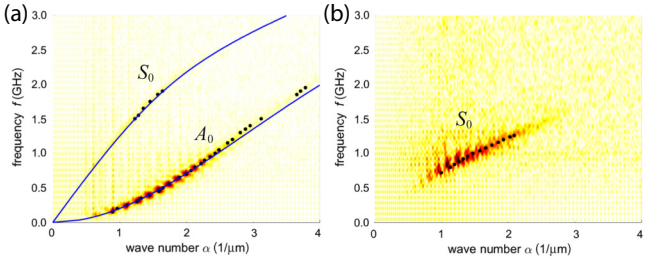

FIG. 5. MPM points obtained using the same measurement data as for the H-functions in Fig. 4 (dark markers). The solid lines in panel (a) are theoretical dispersion curves calculated with the restored effective parameters of the free membrane given in Table I.

correct eigenvalues can be found, while the remaining roots are induced by noise. To filter them, we first use a double-sided MPM scheme proposed in Ref. [18]. It is based on the fact that the eigenvalues μ_n of the matrix pencil $\mu V_1 - V_0$ must be equal to $1/\lambda_n$. The extra roots associated with the noise are unstable, and we discard those from λ_n that do not satisfy the condition $|(\lambda_n - 1/\mu_m)/\lambda_n| < \delta$ for all m with some threshold level δ providing adequate accuracy. We also tried other root selection methods, such as those based on singular-value decomposition or on additional filtering using the H-function. They gave roughly the same results.

These rather strict conditions allowed only a few points $(\zeta_n^{\exp}, f_n^{\exp})$ to be selected, but they proved sufficient to identify the effective material parameters of the free membrane, as well as the average mass of particles deposited on it. Figure 5 gives examples of such MPM-obtained points for the free and heavily loaded samples.

The averaged areal mass m in the sample loaded with nanoparticles can now be estimated by fitting the theoretical dispersion curves with the experimental points, e.g., MPM points in Fig. 5(b). However, the effective input parameters of the free membrane itself must be determined first. According to the previously developed technique [15,19], they are determined by minimizing the objective function

$$F(C, \rho, h) = \sum_n |K_{ij}^{-1}(\zeta_n^{\exp}, f_n^{\exp})| \tag{6}$$

by varying its parameters (the arrays of elastic moduli C, densities ρ, and thicknesses h of the bilayer membrane waveguide). The elements of matrix K are calculated here at the points $(\zeta_n^{\exp}, f_n^{\exp})$ extracted from the experimental data. In accordance with the dispersion equation (3), the magnitude of these elements tends to zero as the varied parameters approach the effective parameters, providing the same calculated GW characteristics as in the measured wave field. To identify the effective parameters of the free membrane, the points shown in Fig. 5(a) were taken as K_{ij} arguments in the goal function in Eq. (6).

TABLE I. Effective input parameters of the free membrane bilayer.

k	Sublayer	E_k (GPa)	μ_k (GPa)	ρ_k (10^3 kg/m^3)	h_k (μm)
1	Au	78.9	27.8	19.3	0.0993
2	Si_3N_4	437	250	3.23	0.527

In the present case, the two densities and the mechanical parameters of the first sublayer (Au) were taken from the literature, so we only varied the thicknesses h_k, $k = 1, 2$, Young's modulus E_2, and shear modulus μ_2 of the second sublayer (Si_3N_4). The complete set of effective input parameters determined in this way is given in Table I.

To assess the average mass of surface particles, a model is needed that takes into account their response to surface displacement and, as a consequence, their influence on the GW dispersion characteristics.

V. EFFECT OF NANOPARTICLE MASS

Mathematical models of GW propagation use the free-surface boundary condition $\boldsymbol{\tau}|_{z=0} = 0$, where $\boldsymbol{\tau} = (\tau_{xz}, \sigma_z)$ is the stress vector on a horizontal surface. Because of Newton's second law, the force response of surface-bound nanoparticles to surface displacement is $\mathbf{F} = M\mathbf{a}$, where M is the total mass of particles on an elementary surface area S, and $\mathbf{a}$ is the averaged acceleration vector of its points. With the steady-state time-harmonic oscillation, $\mathbf{a} = -\omega^2\mathbf{u}$, and dividing Newton's law formula by the area S, this leads to the modified surface boundary condition

$$\boldsymbol{\tau}|_{z=0} + m\omega^2\mathbf{u} = \mathbf{q}, \tag{7}$$

where $m = M/S$ is the averaged areal mass density (pg/μm^2). The use of Eq. (7) instead of the conventional boundary condition $\boldsymbol{\tau}|_{z=0} = \mathbf{q}$, occurring at $m = 0$, leads to a small modification in the algorithm [14] for the matrix K calculation. In other respects, the representations in Eqs. (1) and (2) remain the same. The effect of the areal mass m on the GW propagation is illustrated by the theoretical dispersion curves $f = f_n(\alpha)$ calculated for the unloaded ($m = 0$) and loaded ($m = 1, 2, 4$) samples (Fig. 6).

This model makes it possible both to study the effect of the areal mass m on the SAW dispersion curves, as in Fig. 6, and, conversely, to restore the value of m by fitting the theoretical curves to the points $(\zeta_n^{\exp}, f_n^{\exp})$ experimentally obtained for the samples with particles. In the latter, the effective parameters of the reference free membrane are used for the two-layer waveguide, while the areal mass m is the only parameter varied. For the heavily loaded sample, this resulted in a mean value of $m = 3.57$ pg/μm^2.

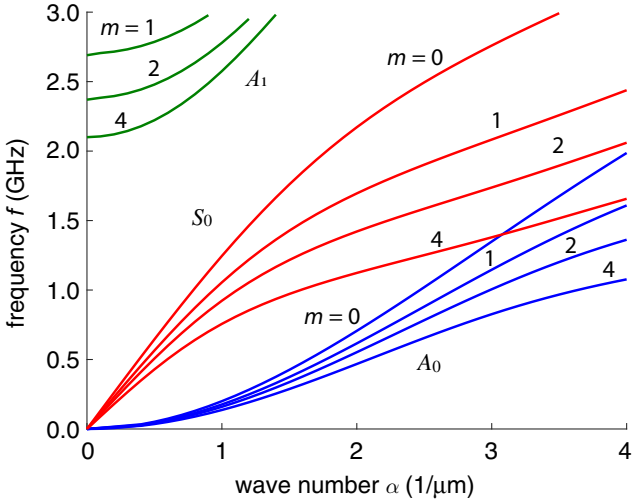

FIG. 6. Effect of surface mass on the GW dispersion curves calculated for $m = 0$, 1, 2, and 4 pg/μm^2 (A_0, S_0, and A_1 modes—blue, red, and green lines, respectively).

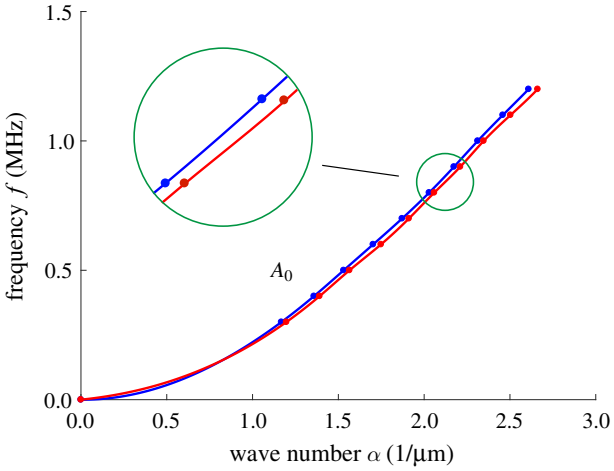

FIG. 8. Dispersion curves of the A_0 fundamental mode (solid lines) drawn through the MPM-obtained experimental points ($\zeta_n^{\text{exp}}, f_n^{\text{exp}}$) (markers) for the free (blue) and slightly loaded (red) membranes.

In Fig. 7, the dispersion curves calculated with such m are drawn over the image of the corresponding H-function [see Fig. 4(b)]. One can see that, unlike the free membrane [Fig. 5(a)], only the mode S_0 is detected in such a heavily loaded waveguide with an amplitude sufficient to be distinguishable in Fig. 7. This behavior can be explained by the different natures of the two guided modes. When the surface of the membrane is loaded with an increasing mass of nanoparticles, the effective areal density of the system rises. The flexural (antisymmetric) A_0 mode, whose dynamics are governed primarily by bending rigidity, is particularly sensitive to such added mass. As a result, its oscillation amplitude decreases much more rapidly than that of the S_0 mode, which is dominated by in-plane stretching and therefore less affected by surface loading. Consequently, the A_0 mode becomes undetectable once its amplitude falls below the sensitivity threshold of the measurement setup, even though it still propagates with dispersion characteristics consistent with theoretical predictions.

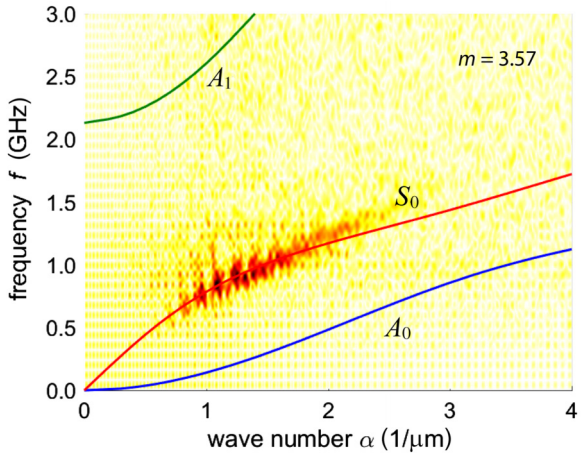

FIG. 7. Dispersion curves calculated for the averaged mass $m = 3.57$ pg/μm^2 MPM-obtained from the experimental data for the heavily loaded membrane; the curves are put on its H-function [Fig. 4(b)].

Obviously, the model cannot directly give the exact mass of discrete particles without some calibration, taking into account the average number of particles in one dose of dispersion, and a series of measurements with various doses. Nevertheless, already now the variation of the areal mass m obtained from the data of picosecond measurements can indicate changes in the number of particles. Consequently, successive measurements over small localized areas make it possible to estimate a spatial gradient of particle density.

To assess the mass resolution provided by this method, we compared the MPM points for the free and slightly loaded samples, the H-functions of which looked almost identical. Nevertheless, the MPM points of these samples turned out to be sufficiently different to be able to distinguish the dispersion curves and estimate the areal mass of nanoparticles on the slightly loaded membrane as $m = 0.155$ pg/μm^2 (Fig. 8).

VI. CONCLUSIONS

The developed method of mass characterization of nanoparticles on micron-thin membranes includes the following stages.

(1) Application of the laser picosecond acoustics technique to obtain the dispersion characteristics of surface acoustic waves propagating over a reference free

membrane and a membrane with surface-distributed nanoparticles. Discrete Fourier transform of the measurement data from the space-time domain to the wave number-frequency domain, and application of an improved MPM scheme to get stable experimental points of GW dispersion curves.

(2) Green's-matrix-based semianalytical simulation of GW propagation in free and mass-loaded bilayer elastic waveguides.

(3) Restoration of effective parameters of the free membrane by minimizing the objective function in Eq. (6), which fits the calculated GW characteristics to the experimentally obtained points.

(4) Estimation of the effective areal mass by fitting the calculated GW characteristics to the experimentally obtained points for the mass-loaded membrane.

The measurement method, which has the advantage of studying a large field of view, is also indirectly influenced by the materials: the membranes are quite expensive and the quality of their surface plays a significant role in the accuracy of measurements. However, in this method, the particles whose mass needs to be estimated can also be deposited on the nonmetallized side of the membrane. In this way, the test laser does not come into contact with the particles and scattered surface waves, facilitating the reception of a clearer acoustic signal.

It should also be noted that the application of the developed theoretical model is not limited to the considered case of a freely supported waveguide (a free bilayer waveguide). Since it works in the general case of a multilayer plate or half-space with arbitrarily anisotropic sublayers [14], the method can be used to estimate the average mass of nanoparticles on samples with different structure, including those placed on an elastic or rigid substrate. Test calculations show the same degree of particle mass influence on surface waves excited in a multilayer half-space or a bottom-clamped layer as in a free waveguide, e.g., as shown in Fig. 6.

In summary, this picosecond acoustic technique ensures sample integrity, facilitates the analysis of delicate materials, and expands its applicability to a diverse array of systems. The method combines experimental precision with advanced mathematical modeling, offering a versatile, noninvasive tool for nanoscale characterization. The study also underscores the importance of integrating theoretical models with innovative experimental methods to bridge gaps in nanoscale research, opening new possibilities for studying mass measurements and other nanoscale phenomena.

ACKNOWLEDGMENTS

The experimental part of this work was supported by the HORIZON EIC Grants DYNAMO (Grant No. 101046489), and the mathematical and computer simulation part was supported by the Russian Science Foundation (Project No. 24-11-00140). This research was also supported by the Spanish Agencia Estatal de Investigación (MICIU/AEI/10.13039/501100011033) through the I+D+I project CEX2023-001263-S (Spanish Severo Ochoa Centre of Excellence program). The authors extend their gratitude to B. Perrin for insightful discussions and invaluable advice throughout this research, as well as to E. Dandeu for clean-room characterization.

DATA AVAILABILITY

The data that support the findings of this article are not publicly available upon publication because it is not technically feasible and/or the cost of preparing, depositing, and hosting the data would be prohibitive within the terms of this research project. The data are available from the authors upon reasonable request.

[1] L. Reimer, *Transmission Electron Microscopy: Physics of Image Formation and Microanalysis* (Springer, Berlin, 2013), 2nd ed.

[2] J. I. Goldstein, D. E. Newbury, D. C. Joy, C. E. Lyman, P. Echlin, E. Lifshin, L. Sawyer, and J. R. Michael, *Scanning Electron Microscopy and X-Ray Microanalysis* (Springer, New York, 2018).

[3] X. Qiao, X. Zhang, Y. Tian, and Y. Meng, Progresses on the theory and application of quartz crystal microbalance, Appl. Phys. Rev. **3**, 031106 (2016).

[4] H. G. Tompkins and W. A. McGahan, *Spectroscopic Ellipsometry and Reflectometry: A User's Guide* (Springer, New York, 2005).

[5] S. Thomas, M. Cole, F. H. Villa-López, and J. W. Gardner, High-frequency surface acoustic wave resonator-based sensor for particulate matter detection, Sens. Actuators A: Phys. **244**, 138 (2016).

[6] J. Liu, W. Hao, M. Liu, Y. Liang, and S. He, A novel particulate matter 2.5 sensor based on surface acoustic wave technology, Appl. Sci. **8**, 82 (2018).

[7] J. Zheng, J. Zhou, P. Zeng, Y. Liu, Y. Shen, W. Yao, Z. Chen, J. Wu, S. Xiong, Y. Chen, X. Shi, J. Liu, Y. Fu, and H. Duan, 30 GHz surface acoustic wave transducers with extremely high mass sensitivity, Appl. Phys. Lett. **116**, 123502 (2020).

[8] F. Xu, L. Belliard, D. Fournier, E. Charron, J.-Y. Duquesne, S. Martin, C. Secouard, and B. Perrin, Complete elastic characterization of lithium phosphorous oxynitride films using picosecond ultrasonics, Thin Solid Films **548**, 366 (2013).

[9] M. Matsukawa, P.-K. Choi, K. Nakamura, H. Ogi, and H. Hasegawa, *Ultrasonics: Physics and Applications* (IOP Publishing, Bristol, 2022).

[10] T. Tachizaki, T. Muroya, O. Matsuda, Y. Sugawara, D. H. Hurley, and O. B. Wright, Scanning ultrafast Sagnac interferometry for imaging two-dimensional surface wave propagation, Rev. Sci. Instrum. **77**, 043713 (2006).

[11] O. Matsuda, M. C. Larciprete, R. L. Voti, and O. B. Wright, Fundamentals of picosecond laser ultrasonics, Ultrasonics **56**, 3 (2015).
[12] Silson. Standard Silicon Nitride Membranes, https://www.silson.com/product/silicon-nitride-membranes/.
[13] W. Stöber, A. Fink, and E. Bohn, Controlled growth of monodisperse silica spheres in the micron size range, J. Colloid Interface Sci. **26**, 62 (1968).
[14] E. Glushkov, N. Glushkova, and A. Eremin, Forced wave propagation and energy distribution in anisotropic laminate composites, J. Acoust. Soc. Am. **129**, 2923 (2011).
[15] E. V. Glushkov, N. V. Glushkova, O. A. Ermolenko, and A. M. Tatarinov, Study of ultrasonic guided wave propagation in bone composite structures for revealing osteoporosis diagnostic indicators, Materials **16**, 6179 (2021).
[16] D. Alleyne and P. Cawley, A two-dimensional Fourier transform method for the measurement of propagating multimode signals, J. Acoust. Soc. Am. **89**, 1159 (1991).
[17] T. K. Sarkar and O. Pereira, Using the matrix pencil method to estimate the parameters of a sum of complex exponentials, IEEE Antennas Propag. Mag. **37**, 48 (1995).
[18] O. L. Ibryaeva and D. D. Salov, Modification of the matrix pencil method using a combined evaluation of signal poles and their inverses, Bull. South Ural State Univ. Ser. Comput. Math. Softw. Eng. **6**, 26 (2017).
[19] E. Glushkov, N. Glushkova, B. Bonello, L. Lu, E. Charron, N. Gogneau, F. Julien, M. Tchernycheva, and O. Boyko, Evaluation of effective elastic properties of nitride NWs/polymer composite materials using laser-generated surface acoustic waves, Appl. Sci. **8**, 2319 (2018).